Advanced Materials Technologies

ADVANCED MATERIALS TECHNOLOGIES
www.advmattechnol.com

RESEARCH ARTICLE OPEN ACCESS

In Situ Integrated Titanium Oxide Synaptic Phototransistor Enabling Multimodal Plasticity and Noise-Robust Selective Attention

Youngbin Yoon[1] | Jaehee Lee[1,2] | Jeongwook Kwon[3] | Yongki Kim[3] | Myunghun Shin[3] | Jung Wook Lim[1,2]

[1]Next-Generation Semiconductor Device Research Section, Electronics and Telecommunications Research Institute (ETRI), Yuseong-gu, Daejeon, Republic of Korea | [2]Department of Semiconductor and Advanced Device Engineering, University of Science and Technology (UST), Yuseong-gu, Daejeon, Republic of Korea | [3]School of Electronics and Information Engineering and Interdisciplinary Program in Space Systems Engineering, Korea Aerospace University, Goyang, Republic of Korea

Correspondence: Jung Wook Lim (limjw@etri.re.kr)

Received: 19 February 2026 | **Revised:** 9 June 2026 | **Accepted:** 16 June 2026

Keywords: associative learning | in situ integration | noise-robust learning | selective attention | UV–electric multimodal synapses

ABSTRACT

Multimodal synaptic plasticity with temporal responsiveness is essential for the construction of energy-efficient neuromorphic systems that emulate biological learning. However, conventional synaptic transistors are often incompatible with multiple stimuli or require complex fabrication processes, limiting their integration into scalable hardware. This paper presents an in situ integrated $TiO_2/SiO_x/Al_2O_3$ synaptic phototransistor that supports UV–electrically coupled plasticity and temporal learning dynamics. This sequential in situ process ensures atomically sharp interfaces, and CMOS-compatible scalability, enabling UV–electrically coupled plasticity and temporally adaptive learning dynamics. The device exhibits robust bidirectional conductance tuning under electrical gating and UV exposure and synergistic modulation when stimuli are applied in combination. Temporal pairing of dual stimuli emulates spike-timing-dependent plasticity and enables associative learning, inspired by insect sensory fusion mechanisms involving electrical and optical cues. Furthermore, a system-level evaluation integrating the device's synaptic characteristics into a spiking neural network shows improved robustness to noise under challenging conditions, highlighting the device's potential to emulate biologically inspired selective attention. Our results create a scalable and versatile synaptic platform that bridges material-level integration with system-level functionality, providing a hardware foundation for energy-efficient and noise-resilient intelligent systems.

1 | Introduction

Neuromorphic electronics aims to emulate the structure and function of biological neural networks and offers a breakthrough in the fields of edge artificial intelligence, real-time sensory computing, and energy-efficient information processing [1–3]. Among the various device architectures, photonic synaptic transistors have attracted great interest due to their capability to process both electrical and optical stimuli. They enable multimodal learning capabilities that are essential for bioinspired hardware systems [4–8]. However, most reported photonic synaptic devices suffer from fundamental limitations such as non-monolithic fabrication, low scalability, and incomplete integration of electrical–optical plasticity [9–11]. In particular, many demonstrations rely on heterogeneous material systems, such as perovskites, 2D semiconductors, or organic–inorganic hybrids, which are often incompatible with CMOS processes and suffer from poor uniformity, ultimately limiting their suitability for large-scale integration

[11–13]. Moreover, synaptic behavior in these systems is typically governed by ion migration [14, 15] or uncontrolled defect-mediated dynamics [16–19], resulting in low reliability, limited endurance, and insufficient control over temporal learning rules such as spike-timing-dependent plasticity (STDP). Moreover, optical and electrical synaptic mechanisms have been studied predominantly in isolation, and few neuromorphic devices have successfully demonstrated their functional integration to exploit potential synergistic effects. This gap emphasizes the need for synaptic platforms that can unify multimodal stimuli within a single device architecture. Beyond serving as a biologically inspired modality, ultraviolet input provides high-contrast and low-background salience cues that are highly relevant for edge-intelligence tasks such as contamination inspection and micro-robot navigation, thereby offering a practical rationale for incorporating UV as a complementary channel to electrical stimulation.

In this study, a consecutively integrated $TiO_2/SiO_x/Al_2O_3$ synaptic phototransistor, was presented in which all functional layers are sequentially deposited in situ using plasma-enhanced atomic layer deposition (PEALD). This approach ensures atomically sharp interfaces and compatibility with wafer-scale processes. The TiO_2 channel layer provides strong responsivity to near ultraviolet (NUV) light, while the engineered SiO_x dielectric facilitates analog conductance tuning through gate-induced charge trapping and de-trapping [20–23]. The underlying Al_2O_3 layer acts as a high-k insulator, minimizing leakage current and stabilizing the electric field across the stack. The TiO_2 channel serves as a UV-sensitive oxide semiconductor that couples photoconductive modulation with gate-controlled charge-trapping dynamics in the $TiO_2/SiO_x/Al_2O_3$ stack. Compared with representative In_2O_3-[24–26], ZnO-[27, 28], and Ga_2O_3-[8, 29–32] based synaptic transistors, this TiO_2 platform integrates optical and electrical plasticity in a monolithic oxide architecture, enabling bidirectional conductance modulation, STDP, associative learning, and system-level noise-robust perception, as summarized in Table S1.

The device exhibits (i) bidirectional synaptic weight modulation under gate voltage pulses, (ii) UV-stimulated potentiation for optically driven learning, (iii) programmable synaptic strength via cumulative dual-stimulus control, and (iv) time-dependent synaptic updates that emulate STDP-like behaviors. Inspired by the sensory fusion mechanisms observed in insect learning, the device mimics associative conditioning through temporally coordinated UV-electric stimuli. These capabilities are achieved within a single, integrated process. In addition to these device-level demonstrations, the evaluation to the system level was extended by integrating experimentally characterized synaptic dynamics into a spiking neural network (SNN), confirming noise-robust classification and functionality similar to selective attention.

These results suggest that the proposed platform can serve as a foundation for hardware-implemented noise-resilient perception inspired by biological systems [33–35]. Such capability is essential for future bio-inspired smart sensors and edge neuromorphic platforms, where robust operation under noisy environments is critical [36]. By unifying multimodal plasticity, temporal learning dynamics, and selective attention-like behavior in a scalable device architecture, this work helps bridge the gap between material-level advances and system-level neuromorphic functionality, complementing recent developments in both biological research and attentional mechanisms in deep neural networks (DNNs) [37, 38]. This capability positions the device as a promising hardware platform for future bio-inspired smart sensors and edge neuromorphic systems that require robust operation in real-world noisy environments.

The remainder of this paper is organized as follows. Section 2 presents the results and discussion, highlighting the device characteristics, multimodal synaptic plasticity, and system-level evaluations. Section 3 summarizes the main conclusions and broader implications of this work. Section 4 describes the experimental methods, including device fabrication, characterization, and evaluation using learning models.

2 | Results and Discussion

The synaptic phototransistor proposed in this study is designed to respond to optical and electrical stimuli. It is based on a TiO_2-channel field-effect transistor (FET) with a dual-gate dielectric stack, as illustrated in Figure 1a. The device has a bottom-gate architecture with TiO_2 as the semiconducting channel layer, a charge-inducing dielectric (CID), and an Al_2O_3 bottom dielectric. All functional layers were deposited sequentially in the same chamber using PEALD, which enables in situ growth and ensures excellent interface quality. This fabrication method ensures uniform film coverage and stable electrical characteristics, which are particularly important for analog synaptic operation. To evaluate the practical uniformity of the devices, transfer characteristics and statistical distributions of threshold voltage and field-effect mobility were extracted from 50 $TiO_2/SiO_x/Al_2O_3$ transistors randomly selected from different locations across a 6-inch wafer, showing reasonably uniform electrical characteristics with mean values of 1.05 V and 4.41 $cm^2/V{\cdot}s$ and coefficients of variation of 17.27% and 20.84%, respectively, as summarized in Figure S1. Long-term storage stability was also examined by comparing transfer characteristics measured immediately after fabrication and after 2 years of storage. The devices retained stable transistor operation after 2 years under ambient laboratory storage conditions, with the threshold voltage moderately shifting from 0.85 to 1.17 V and the field-effect mobility largely maintained from 4.65 to 4.36 $cm^2/V{\cdot}s$, corresponding to approximately 94% of the initial mobility.

Figure 1a schematically outlines the operating concept of the TiO_2-based synaptic phototransistor. In biological systems, synapses serve as junctions between neurons, and the strength of the connection is modulated by the history of presynaptic activity. Presynaptic spikes, triggered by external stimuli, release neurotransmitters that generate a postsynaptic current (PSC) in the adjacent neuron. This PSC is a core element of synaptic signal transmission and plasticity and can be emulated by optically or electrically induced current in the device. Before evaluating the synaptic behavior, the basic electrical characteristics of the TiO_2-based FET were evaluated. Figure 1b shows the transfer characteristics measured at 300 K, obtained by sweeping the gate voltage (V_G) forward and reverse while the drain voltage (V_D) was fixed at 1 V. The I_D–V_G curve shows a gate modulation ratio of approximately 10^6 during the forward sweep.

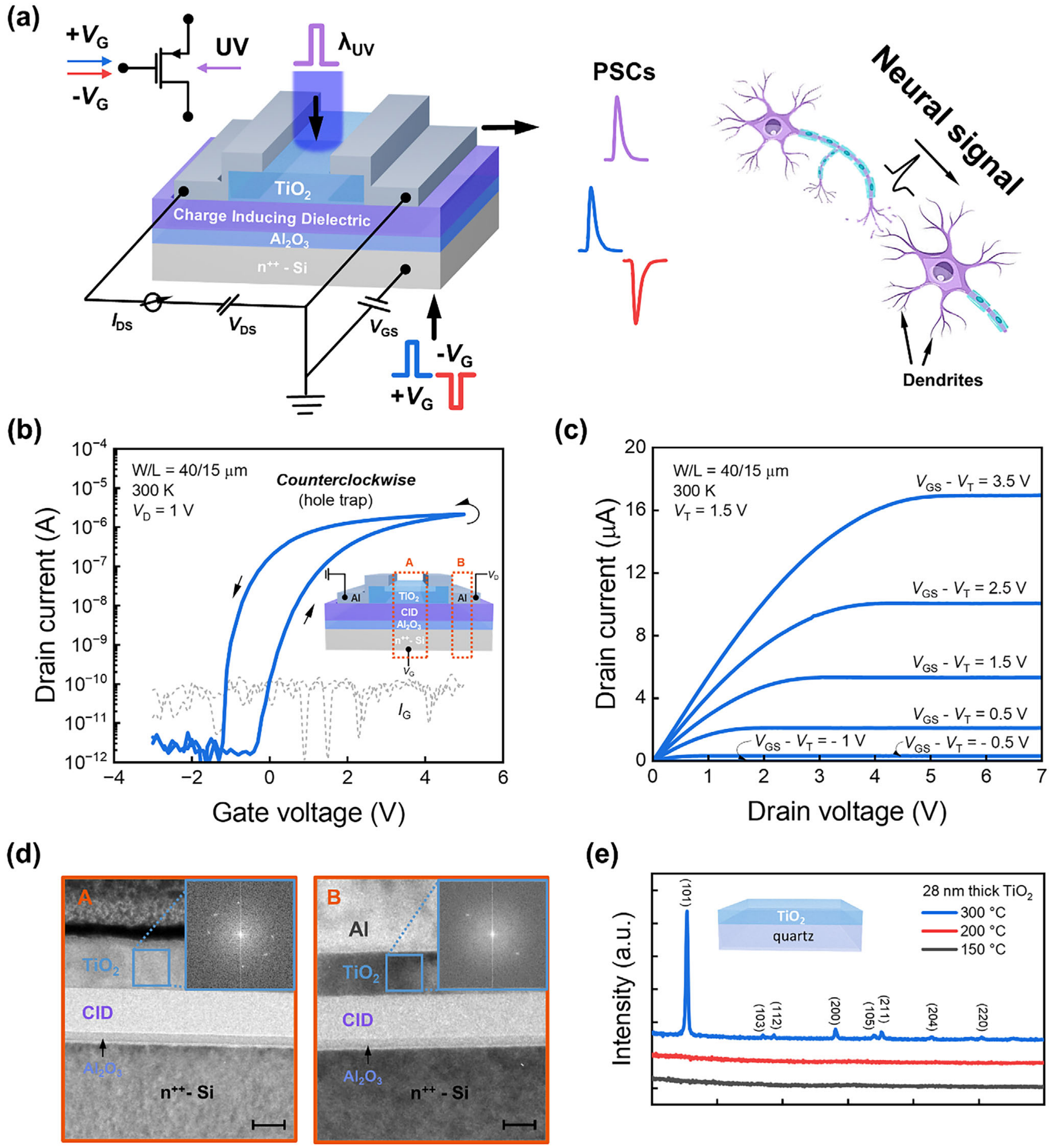

FIGURE 1 | TiO_2-based synaptic phototransistor responsive to hybrid optical/electrical stimuli. (a) Schematic representation of the synaptic phototransistor operating under both optical and electrical stimulation. (b) Transfer characteristics (I_D–V_G) measured under dark conditions during a V_G sweep from −3 to 5 V and back to −3 V. (c) Output characteristics (I_D–V_D) of the device. *Inset in (b)*: Schematic cross-sectional of the device structure. (d) TEM cross-sectional images of regions A and B, as marked in the inset of (b), used to analyze layer thicknesses, crystallinity, and interface quality. *Insets*: Corresponding fast Fourier transform (FFT) patterns (scale bar: 20 nm). (e) X-ray diffraction (XRD) patterns of 28 nm-thick TiO_2 films deposited at 150°C, 200°C, and 300°C.

The presence of the CID layer, which was developed to generate synaptic-like memory effects, plays a crucial role in this behavior. The CID layer consists of an oxygen-excessive composition that violates the stoichiometry of silicon oxide films by optimizing the PEALD process parameters. The ALD process enables atomic-level film deposition and relatively free control of the chemical composition. The oxygen-excessive composition of the silicon oxide causes the material to exist in an excess hole state. The related results have been demonstrated in our previous studies [20–23, 39]. Excess holes are trapped at the interface between

TiO_2 and CID during the forward sweep and locally modulate the channel conductance. When the sweep is reversed, these trapped positive charges act as an additional gate bias, shifting the threshold voltage (V_{th}) in the negative direction and resulting in a counterclockwise hysteresis loop, as depicted in Figure 1b. The CID layer should not be regarded as a finite hole reservoir that is irreversibly depleted during device operation. Instead, the counterclockwise hysteresis is attributed to reversible trapping and de-trapping of positive trapped-charge states near the TiO_2/CID interface, which modulate the channel conductance during bias application and gradually relax after bias removal. Details of the CID deposition process can be found in the Experimental Section. Figure 1c presents the output characteristic of the device. It shows a well-defined linear region and pinch-off in a saturation region corresponding to the typical behavior of an n-type semiconductor. This confirms stable electron conduction in the TiO_2 channel and highlights the feasibility of precise current control, which is essential for the implementation of synaptic weight modulation in neuromorphic hardware.

Cross-sectional transmission electron microscopy (TEM), as shown in Figure 1d, was used to analyze the structural features of the device. Regions A and B, highlighted in the schematic inset of Figure 1d, show uniform and damage-free deposition of TiO_2, CID, and Al_2O_3 layers grown consecutively by PEALD. The measured thicknesses were approximately 28 nm for TiO_2, 25 nm for the CID layer, and 5.5 nm for Al_2O_3. Fast Fourier transform (FFT) diffraction patterns obtained from both regions yielded lattice spacings of 3.513 and 3.52 Å, both corresponding to the (101) crystallographic plane of anatase-phase TiO_2 based on the JCPDS reference file No. 00-021-1272. The anatase phase, which has superior semiconducting properties compared to rutile or amorphous TiO_2, phases that typically exhibit low carrier mobility or insulating behavior generally forms within a narrow temperature window [40]. Therefore, precise optimization of the fabrication conditions that promote anatase formation is essential for obtaining high-quality semiconducting films. In this study, the anatase phase was selectively formed by carefully adjusting the PEALD deposition temperature within this critical range. Figure 1e shows x-ray diffraction (XRD) patterns of 28 nm-thick TiO_2 films deposited at different PEALD temperatures to verify this phase formation. No distinct diffraction peaks were observed at 150 and 200°C, while a sharp peak appeared at 300°C, consistent with the anatase (101) reflection. This observation is consistent with both the TEM-FFT analysis and previous reports on the crystallization behavior of the anatase phase [41, 42].

These results confirm the successful fabrication of a synaptic phototransistor in which the TiO_2 channel and the two dielectric layers are grown sequentially in a single PEALD chamber, forming an in situ integrated active stack with high structural integrity. In the following sections, the optoelectronic properties of TiO_2 and the synaptic response behavior under optical and electrical stimulation are investigated.

The optical properties of the optimized TiO_2 thin films and the photo response characteristics of the fabricated synaptic phototransistor are shown in Figure 2. Figure 2a shows the transmittance spectrum of a 28 nm-thick TiO_2 film deposited on a quartz substrate. The films exhibit over 70% transmittance in the visible range, which is consistent with the typical behavior of TiO_2 thin films [43]. Based on the measured transmittance and the Tauc plot method, the optical bandgap of the TiO_2 film was estimated to be 3.26 eV, as shown in Figure 2b. As TiO_2 is known to have an indirect bandgap in the anatase phase [40], the bandgap was extracted using the indirect transition model in the Tauc formalism. From the extracted bandgap value, it can be deduced that incident light with a wavelength of approximately 380 nm or shorter is required to excite the photocarriers in the TiO_2 layer via band-to-band excitation. It is also worth noting that if radiative defect states exist within the bandgap, sub-bandgap illumination—that is, light with a wavelength longer than 380 nm—may still trigger partial photocarrier generation. Furthermore, as shown in Figure 2b, an absorption tail is observed below the 3.2 eV region, indicating the presence of sub-bandgap absorption. This behavior may be attributed to defect-induced states or localized energy levels within the TiO_2 layer. Such behavior has already been reported in a previous study by our group [44]. To further evaluate the photoresponsivity characteristics of the fabricated device, spectral photoresponsivity measurements were performed under different gate bias conditions, as shown in Figure 2c. The device showed maximum responsivity at 220 nm. In view of this result, the optical input wavelength for synaptic stimulation was set to 365 nm. Accordingly, a wavelength of 365 nm was chosen for synaptic stimulation, which is slightly higher than the TiO_2 bandgap energy, as it generates enough photocarriers at the TiO_2/CID interface to ensure stable synaptic operation.

Next, the temporal dynamics of the synaptic response to single optical and electrical pulses were examined, as shown in Figure 2d–f. The duration of each input pulse was fixed at 300 ms, and the V_D was held at 1 V. The initial gate voltage (V_{Gi}) was set to 0.5 V for both optical and electrical stimulation conditions. This value was chosen based on four important considerations. First, the selected V_{Gi} must be within a region where the drain current (I_D) is not affected by the gate leakage current, as shown in the transfer characteristics in Figure 1b. In gate voltage regions where the gate and drain currents are of similar magnitude, the modulation of the channel conductance by gate input becomes less reliable. Second, the V_{Gi} should be near the V_{th} for sufficient modulation margin to ensure synaptic potentiation and depression from the initial state. Third, the current level at V_{Gi} should be high enough to ensure reliable time resolution during measurements. Since the sampling rate of the measurement system is limited by the current level, it was necessary to maintain an initial I_D above 100 nA to accurately capture millisecond-scale biological pulse responses. Finally, low-power operation was also considered. Minimizing power consumption requires both low operating voltage and low current. Considering all four factors and their trade-offs, the optimal V_{Gi} was determined to be 0.5 V. Figure 2d shows the temporal evolution of the drain current in response to a single optical pulse with an intensity (P_{in}) of 1.53 mW/cm^2 and a wavelength of 365 nm. After light stimulation, the drain current increases rapidly and then gradually decays over several minutes after the stimulus is removed. This behavior is analogous to an excitatory postsynaptic current (EPSC) in biological synapses. The optical stimulation mode that elicits this EPSC response is the *L* mode. Figure 2e,f shows the temporal behavior of the synaptic current in response to gate voltage pulses of 5 and 0 V, respectively. Given that the V_{Gi} was set to 0.5 V, the 5 and 0 V pulses correspond to positive and negative pulses

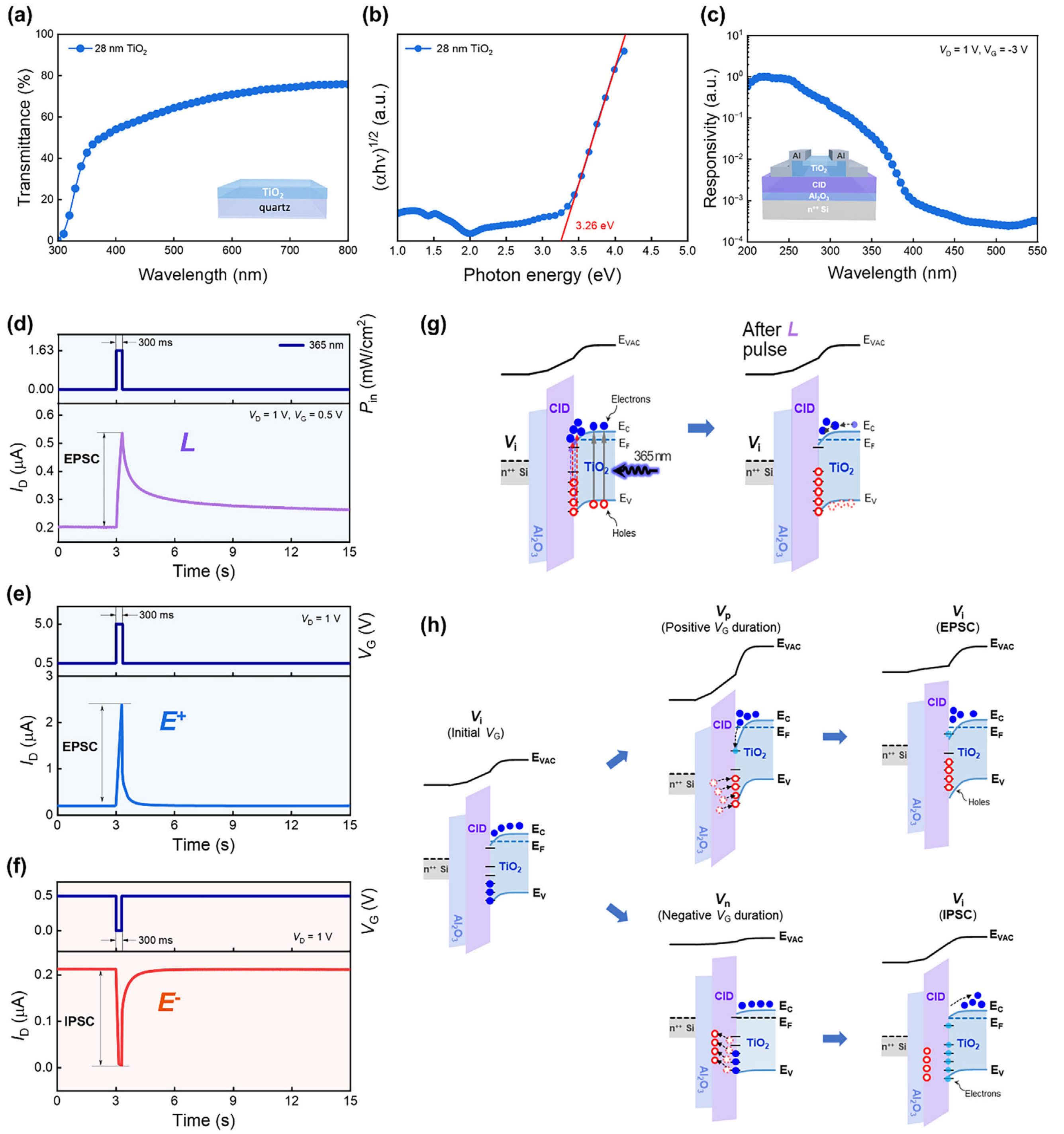

FIGURE 2 | (a) Transmittance spectra and (b) extraction of the optical band gap of TiO_2 (indirect bandgap model) determined by Tauc plots using the transmittance spectra. (c) Spectral photoresponsivity of the TiO_2-based synaptic phototransistor at different gate voltages. (d–f) Current characteristics of a single optical and electrical pulse. Postsynaptic current (PSC) induced by 300 ms optical/electrical pulse stimulation. Synaptic operating principle of the TiO_2 phototransistor response in (g) optical (L) and (h) electrical (E^+, E^-) stimulation mode.

with respect to the baseline; that is, they effectively correspond to the application of +4.5 V and −0.5 V with respect to the V_{Gi}. When a positive pulse is applied, the drain current increases sharply followed by a gradual recovery over several seconds. In contrast, a negative bias pulse results in an immediate drop in current, which also recovers slowly over time. The excitatory response to the positive gate pulse corresponds to an EPSC and is defined as E^+ mode. Conversely, the inhibitory response to the negative gate pulse, which reduces the drain current, mimics an inhibitory postsynaptic current (IPSC) and is defined as the E^- mode. These results confirm that the device can successfully show synaptic potentiation and depression under optical and electrical stimulation.

The underlying mechanisms responsible for the synaptic behavior under each stimulation mode were further investigated.

Figure 2g shows a band diagram model illustrating the mechanism of EPSC observed in L mode. The initial energy band alignment at $V_{Gi} = 0.5$ V is shown on the left. Previous studies have shown that the CID layer introduces dense deep trap states at the TiO_2 interfaces [20–23, 39]. Upon illumination, the TiO_2 channel immediately produces a photocurrent signal, while electrons at the TiO_2/CID interface traps absorb photons, leaving holes in the traps, and the released electrons contribute to the photocurrent in the channel. The trapped holes remain as a persistent positive space charge that attracts channel electrons and maintain the increased drain current (persistent photocurrent) until de-trapping restores the initial state. The duration of the elevated current is governed by the lifetime of the trapped holes (electron restoration), with deeper traps having a longer lifetime. Figure 2h shows the band diagrams corresponding to the synaptic behavior under electrical stimulation modes (E^+ and E^-). When a positive gate pulse (V_p) is applied, positive charges (holes) trapped in the CID layer are driven toward the TiO_2 interface. As a result, the reduced electric field across the CID lowers the energy levels at the CID/ TiO_2 interface, which promotes accumulation of electrons in the TiO_2 channel near the interface, thereby increasing the current (E^+). Conversely, a negative V_p changes the occupancy and spatial distribution of positive trapped-charge states near the TiO_2/CID interface, thereby increasing the electric field across the CID. This raises the interfacial energy levels, reducing electron accumulation and lowering the E^- mode current at the TiO_2 channel. The two-slope current decrease observed during negative gate-pulse application in the E^- mode suggests that multiple kinetic components contribute to the electrical response. Considering the present electrical data, this behavior is conservatively interpreted as field-driven trap-mediated charge redistribution involving energetically and/or spatially distributed interfacial trapped-charge states near the TiO_2/CID interface. After removal of the gate pulse, the delayed current recovery is interpreted as trap-limited charge release associated with deep or energetically distributed trapped-charge states near the TiO_2/CID interface, rather than simple free-hole transport. Carrier emission from deep trap states is a thermally activated process, and its characteristic time constant increases exponentially with trap depth; therefore, such interfacial trapped-charge states can account for the second-scale recovery observed in the electrical stimulation modes.

To quantitatively link the time-extended PSC in Figure 2 to interfacial trapping, we additionally measured sweep-delay (t_d)-dependent hysteresis (Supporting Information S2) and pulse-induced V_T shifts (Supporting Information S3). The S2(a) transfer loop is counter-clockwise, consistent with positively charged, hole-trapping (donor-like) centers at the TiO_2/CID interface [45]. Mechanistically, a forward sweep to positive V_G increases the occupancy of hole traps, shifting V_T negatively and thereby increasing the channel conductance at a given V_G. In our devices, the hysteresis window decreases as the sweep delay increases: during fast sweeps relative to the trap time constants, slow interfacial hole traps cannot equilibrate, so the return trace retains residual positive interfacial charge and yields a larger loop [45, 46]. Increasing the step dwell time allows trap capture/release to relax toward quasi-equilibrium, thereby reducing the residual charge and sharpening the slope near the positive-bias end. Specifically, Supporting Information S2b plots the hysteresis window $|\Delta V_T|$ versus $\log_{10} t_d$, showing a near-linear decrease with increasing dwell time, which directly supports an equilibration-dominated interfacial trapping mechanism [45–47]. S3 compares the fresh state with the threshold shifts measured immediately after applying 50 pulses for the E^+ and E^- stimuli. The equivalent interfacial trapped-charge density N_{trap} at the TiO_2/CID interface was obtained using Equation (1).

$$N_{trap} = \frac{C_{ox,eff}}{q} |\Delta V_T| \tag{1}$$

where ΔV_T is the threshold-voltage change from the fresh state, q is the elementary charge, and $C_{ox,\,eff}$ is the series-equivalent gate capacitance per unit area of the stacked CID/Al_2O_3 dielectrics defined by

$$C_{ox,eff} = \left(\frac{t_{CID}}{\varepsilon_0 \varepsilon_{CID}} + \frac{t_{Al_2O_3}}{\varepsilon_0 \varepsilon_{Al_2O_3}} \right)^{-1} \tag{2}$$

Here, t_{CID} and t_{Al2O3} denote the film thicknesses of the CID and Al_2O_3 layers (25 and 5 nm, respectively); ε_0 is the vacuum permittivity; and $\varepsilon_{CID} = 5.0$, $\varepsilon_{Al2O3} = 9.0$ are the relative permittivities extracted from standalone single-layer MIM test capacitors fabricated in the same deposition runs and conditions as the device layers. Applying Equations (1), (2) gives, for E^+ ($|\Delta V_{T,\,E}{}^+| = 0.26$ V) and E^- ($|\Delta V_{T,\,E}{}^-| = 0.19$), $N_{trap,\,E}{}^+ \approx 2.59 \times 10^{11}$ cm^{-2}, $N_{trap,\,E}{}^- \approx 1.89 \times 10^{11}$ cm^{-2} which are reasonable for oxide TFT interfaces. Considering 50 pulses, the per-pulse trapped-charge densities are 5.18×10^9 cm^{-2} (E^+), 3.78×10^9 cm^{-2} (E^-), supporting reversible conductance tuning of the $TiO_2$$^-$ based synaptic transistor under appropriate gate-pulse programming.

In summary, the synaptic behavior in the optical mode is governed by photogenerated holes supplied directly from the TiO_2 channel. In the electrical mode, the temporally extended current response is governed by trapping and de-trapping of positive trapped-charge states near the TiO_2/CID interface. Both mechanisms lead to temporally extended current responses that mimic biological synaptic functions.

In addition to the synaptic behavior during single-pulse stimulation, one of the main advantages of a three-terminal synaptic device is the ability to fine-tune the synaptic weight. Such precise control enables complex signal processing with temporally varying stimulation. The ability of the TiO_2-based synaptic phototransistor to modulate the connection strength between neurons was investigated by systematically varying the total stimulus dose by controlling of the intensity and duration of the applied stimuli, as shown in Figure 3. The intensity of the optical pulse (P_{in}) and the amplitude of the gate voltage pulse (V_G) were adjusted for optical and electrical stimulation, respectively, and the pulse width was varied to control the stimulus duration. Figure 3a–c shows the temporal evolution of synaptic current in response to varying stimulus strengths and durations under L, E^+, and E^- modes, respectively. More potent stimuli and longer durations consistently led to stronger changes in synaptic current changes in all three modes. This behavior reflects a precise dose-dependent modulation that mimics activity-dependent plasticity similar to biological synapses. Figure 3d compares the values of the resulting postsynaptic current (PSC) as a function of stimulus intensity for each mode. The results show that the synaptic weight can be fine-tuned by adjusting the input strength,

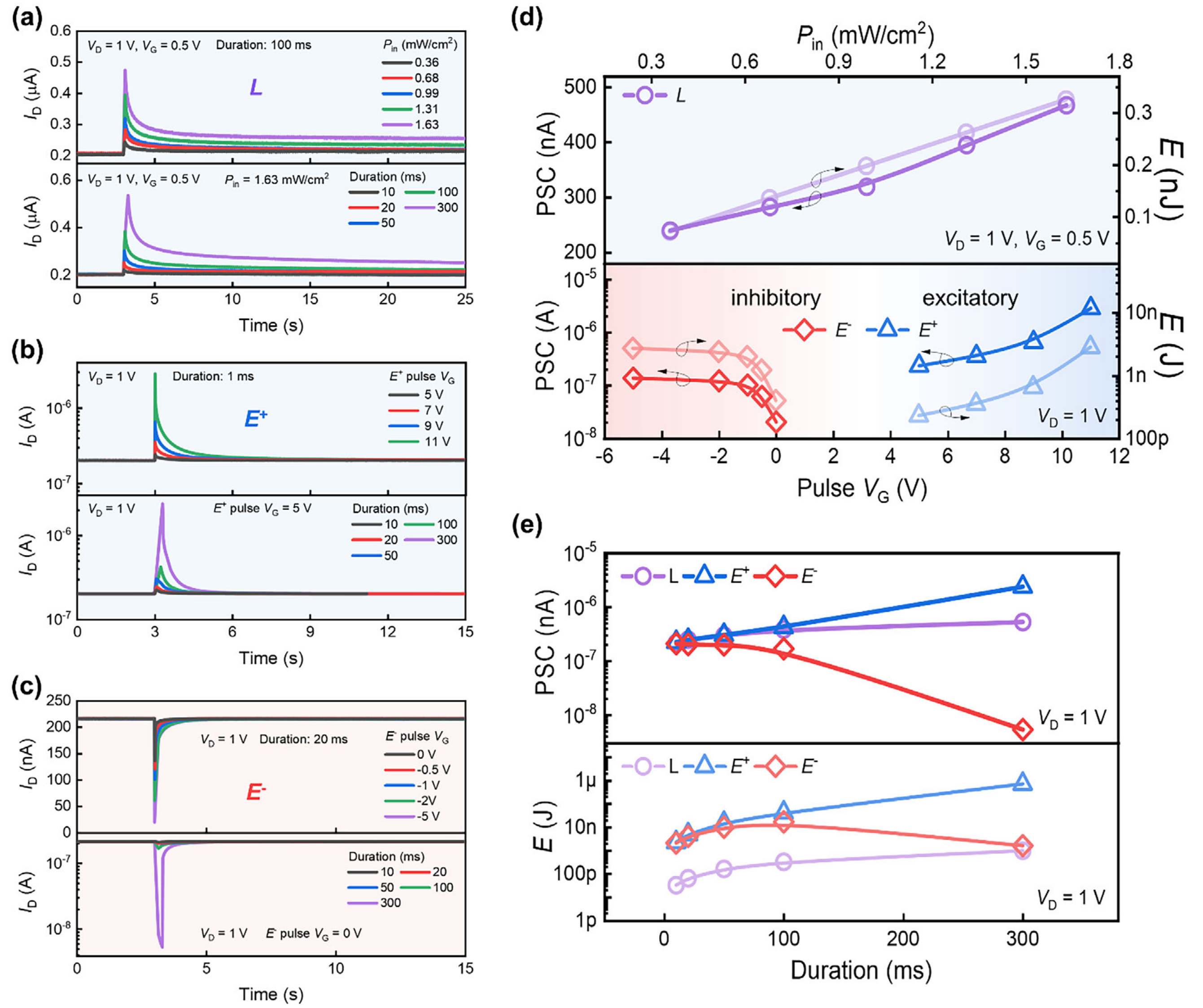

FIGURE 3 | Demonstration of the control of synaptic connection strength by controlling the amount of optical and electrical input stimulation. Time-dependent PSC characteristics under optical and electrical stimulation: drain current of optical pulse power (P_{in}) and duration in (a) L mode and drain current of the electric pulse (V_G) and duration in (b) E^+ and (c) E^- modes. (d) PSC at different simulated optical (P_{in} in L mode) and electrical (V_G in the E^+ and E^- modes) intensities with a fixed duration of 100, 1, and 20 ms, respectively and (e) for different durations of optical and electrical pulses.

allowing precise control of neural activation. Figure 3e shows PSC as a function of pulse duration. In all modes, synaptic current increased exponentially with stimulus duration, indicating strong time-dependent accumulation.

Energy consumption for each stimulation condition assessed operational efficiency. The energy per event was estimated as $dE = S{\cdot}P{\cdot}dt$ for the optical input and $dE = V{\cdot}I{\cdot}dt$ for the electrical input, where S is the effective area of the device exposed to the incident photons, P is optical power density, V is drain voltage, I is drain current, and t is pulse duration [48]. The L mode exhibits pulse energies in the order of below 1 nJ, while the E^+ mode reached the ≈ 10 nJ level due to the higher current flow (Figure 3d). For comparison, biological synapses consume approximately 10 fJ to 1 pJ per event [49]. Although the electrical modes are still several orders of magnitude higher, the optical mode is approaching biologically plausible energy budgets. To further reduce energy consumption, device scaling is an effective approach, as smaller active areas reduce both the optical absorption volume and the electrical drive current. In addition, optimizing the pulse shape and operating at low voltage could help minimize energy loss while maintaining synaptic functionality. These results confirm that the total stimulus dose applied to the TiO_2-based synaptic phototransistor not only modulates synaptic weight with high resolution but also enables a controllable trade-off between energy and performance. This is crucial for scalable, energy-efficient neuromorphic learning systems.

A fundamental requirement for artificial synaptic devices is the ability to emulate both short-term and long-term synaptic plasticity, which is a hallmark of biological neural systems. Short-term plasticity (STP) is a fundamental feature of biological synapses and is closely related to the accumulation of calcium ions at presynaptic terminals. STP in the TiO_2-based synaptic phototransistor was evaluated under all three stimulation modes using

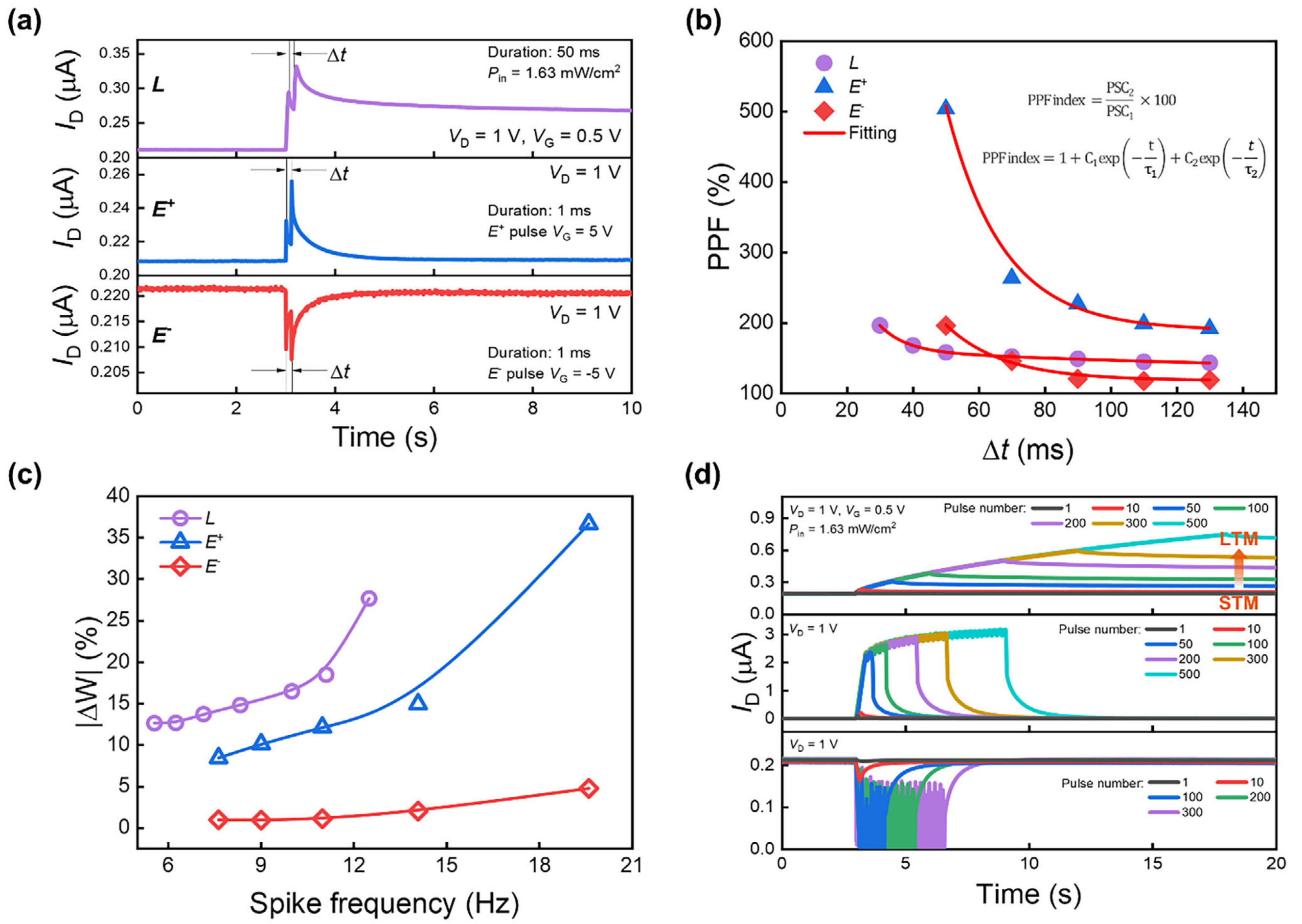

FIGURE 4 | Paired-pulse facilitation (PPF) and weight modulation characteristics of TiO_2-based synaptic phototransistors. (a) Time-dependent I_D behavior under stimulation by consecutive 365 nm ($P_{in} = 1.53$ mW/cm^2) pulses in L mode with Δt and duration of 50 ms. And under stimulation by two consecutive positive and negative V_G pulses in E^+ and E^- modes with a duration Δt of 1 ms. (b) PPF index as a function of Δt for optical and electrical spikes, and (c) $|\Delta W|$ as function of the spike frequency. (d) Time-dependent synaptic current for consecutive spikes in L mode ($P_{in} = 1.63$ mW/cm^2), E^+ mode (pulse $V_G = 5$ V), and E^- mode (pulse $V_G = 0$ V). For all three stimulus modes, the duration and interval are 10 and 12 ms, respectively.

paired-pulse facilitation (PPF), which measures the enhancement of the second synaptic response when two stimuli are applied in rapid succession. Figure 4a shows a representative PPF measurement, in which two input pulses with a defined inter-pulse interval Δt were applied. The resulting temporal evolution of synaptic current was recorded for each mode. Additional data for time-dependent current traces under different Δt values can be found in Supporting Information S4. The PPF index was calculated as the ratio of the peak current induced by the second pulse to the current caused by the first pulse. Figure 4b shows the PPF index plotted as a function of Δt for the L, E^+, and E^- stimulation modes. In all cases, the PPF index increased with decreasing Δt, which is consistent with the STP behavior. To further analyze the memory time and dynamic response speed of the device, the PPF index data were fitted with a double exponential decay function of $PPF = 1 + C_1 \cdot exp(-t/\tau_1) + C_2 \cdot exp(-t/\tau_2)$, where τ_1 and τ_2 represent the fast and slow decay times associated with the decrease in PPF in response to optical and electrical stimuli, respectively. The extracted τ_1 and τ_2 values for each stimulation mode are listed in Table 1. In particular, for optical stimulation mode, τ_1 and τ_2 were 7.9 and 159.7 ms, respectively. These time constants are comparable to the typical time scales of biological synapses, which have both fast (tens of milliseconds) and slow (hundreds of milliseconds) components of facilitation [50]. Figure 4c also shows the absolute value of synaptic weight change ($|\Delta W|$) as a function of spike frequency ($= 1/\Delta t$). All three modes exhibited a frequency-dependent modulation of $|\Delta W|$, indicating that synaptic weight can be significantly tuned by controlling the frequency of the input spikes. Notably, positive pulses under electrical stimulation caused greater changes in synaptic weight than negative pulses, with the optical mode showing the greatest overall modulation. These distinct profiles of weight modulation under different stimulation modes can be strategically exploited to more accurately

TABLE 1 | Decay times of the TiO_2-based synaptic phototransistor extracted by PPF index fitting.

Decay time	τ_1 (ms)	τ_2 (ms)
L	7.9	159.7
E^+	15.2	18.6
E^-	15.5	18.9

emulate the synaptic weight adaptation observed in biological systems.

The ability to emulate long-term plasticity (LTP) was also assessed. In the brain, the hippocampus plays a central role in memory formation, and it is known that the conversion of short-term memory to long-term memory occurs through repeated stimulus rehearsal. To investigate this transition in the TiO_2-based device, the number of input pulses was systematically varied while the synaptic current response was monitored (Figure 4d). Increasing the input pulses in all three stimulation modes resulted in a gradual increase in |PSC| and prolonged retention of the induced current state. This prolonged retention originates from the increasing contribution of persistent trapped charge under repeated stimulation. Repeated pulses promote the occupation and relaxation of long-lived trapped charge states near the TiO_2/CID interface, thereby delaying the post-stimulus recovery of the channel conductance. To quantify this behavior, an effective decay time constant (τ) was extracted by fitting the post-stimulus current relaxation with a single-exponential function. The extracted τ values increased from 0.57 to 3.32 s in the L mode, from 0.03 to 0.53 s in the E^+ mode, and from 0.38 to 0.49 s in the E^- mode, confirming that the increase in decay duration is most pronounced in the L mode and smaller but still observable in the E^+ and E^- modes (Supporting Information S5). These observations support the successful emulation of long-term memory formation by repetitive stimulation.

In summary, the TiO_2-based synaptic phototransistor was able to replicate both short-term and long-term synaptic plasticity. These results improve the biorealism of artificial synapses and support the development of neuromorphic devices that better mimic biological information processing.

LTP serves as a fundamental mechanism underlying learning and memory in biological synapses, and its hardware emulation is essential to enable autonomous learning in neuromorphic systems. Among the various plasticity rules, STDP provides a biologically realistic framework by modulating synaptic strength based on the precise timing between pre- and post-synaptic spikes [51]. The implementation of STDP is particularly important to enable learning algorithms in spiking neural networks (SNNs).

As shown in Figure 5, STDP behavior was systematically characterized for four different stimulus combinations. Additional data for time-dependent current traces under different Δt values can be found in Supporting Information S6. The Δt ranges in Figure 5a–d were set differently due to limitations in the temporal resolution and dynamic range of the measurement setup. Further evaluations under a unified time scale are warranted to enable a more direct quantitative comparison across all stimulus combinations. This observation is consistent with the Hebbian learning rule, which states that the synaptic strength between two neurons increases when their activations are temporally correlated—often summarized as “cells that fire together, wire together.” To quantitatively model the timing-dependent synaptic plasticity, STDP responses were fitted with an exponential Hebbian function of the form $\Delta W = A \cdot exp(-|\Delta t|/\tau)$, where A denotes the amplitude of synaptic change and τ is the characteristic time constant [52, 53]. This formulation captures the exponential sensitivity of ΔW updates to the Δt between pre- and post-synaptic spikes. Optical-only (L/L), positive electrical (E^+/E^+), and negative electrical (E^-/E^-) stimulus pairs produced symmetrical Hebbian ΔW profiles centered at $\Delta t = 0$ with positive (Figure 5a) and negative (Figure 5b) synaptic weight changes, respectively. These results confirm that all identical modes act as potentiating or depressing stimuli, regardless of the order of pre- and post-synaptic inputs. When comparing the L and E^+ modes, the optical stimulus showed a relatively smaller ΔW variation for the spike timing difference, indicating less sensitivity to temporal asymmetry. In Figure 5b, the E^- mode induced synaptic weakening regardless of the order of the pre- and post-synaptic spikes, which differs from conventional STDP behavior in which both potentiation and depression can occur as a function of spike timing. This difference is likely due to the fact that in this study both pre- and post-synaptic spikes were applied to the gate electrode, whereas conventional synaptic transistors normally deliver them separately to the gate and drain electrodes. In contrast, Figure 5c,d illustrate mixed-mode stimulus conditions. When a positive electrical pulse was paired with an optical stimulus (E^+–L), the STDP response followed a symmetric Hebbian function with positive ΔW values, reflecting the combined potentiating effect of both stimuli. On the other hand, in the E^-–L condition (Figure 5d), the STDP response became asymmetric: positive and negative Δt values for synaptic potentiation and depression, respectively. This asymmetric Hebbian profile implies that the balance between excitatory and inhibitory stimuli governs the direction of synaptic modification. This emphasizes the potential for fine-tuning multimodal temporal learning in artificial synapses. This finding highlights a key advantage of the proposed device: by alternately applying different types of stimuli to the same gate electrode, both synaptic potentiation and depression can be achieved, depending on the stimulus order. This demonstrates that multimodal temporal learning can be finely controlled under a unified input scheme, in which different types of stimuli are funneled into the same gate electrode. This distinguishes our approach from conventional synaptic transistors that distribute inputs across multiple terminals.

The time constants (τ) extracted from the fitted Hebbian functions provide information about the temporal dynamics of synaptic plasticity for different stimulus combinations (Table 2). In symmetric stimulus cases (L/L, E^+/E^+, and E^-/E^-), the τ values show balanced temporal responses and consistent plasticity mechanisms for repeated identical stimuli. Remarkably, the E^-/E^- mode exhibited the shortest τ (~15.7 ms), indicating rapid synaptic depression and faster decay of temporal sensitivity compared to the potentiation modes. In contrast, the mixed stimulus cases showed significant asymmetry in τ values. The E^+/L condition exhibited an extended τ for positive Δt (180.1 ms), implying prolonged temporal sensitivity to potentiation due to the synergistic effect of dual excitatory inputs. Meanwhile, the E^-/L condition showed a highly asymmetric profile with an extremely long τ for negative Δt (1, 184.7 ms), suggesting that inhibitory–excitatory combinations produce sustained temporal windows for depression. These results emphasize the tunability of temporal characteristics of STDP across stimulus modality and provide new degrees of freedom for the development of time-sensitive neuromorphic circuits.

It is noteworthy that the τ values for symmetric stimulus cases (L/L: 22.4 ms, E^+/E^+: 31 ms, and E^-/E^-: 15.7 ms) closely

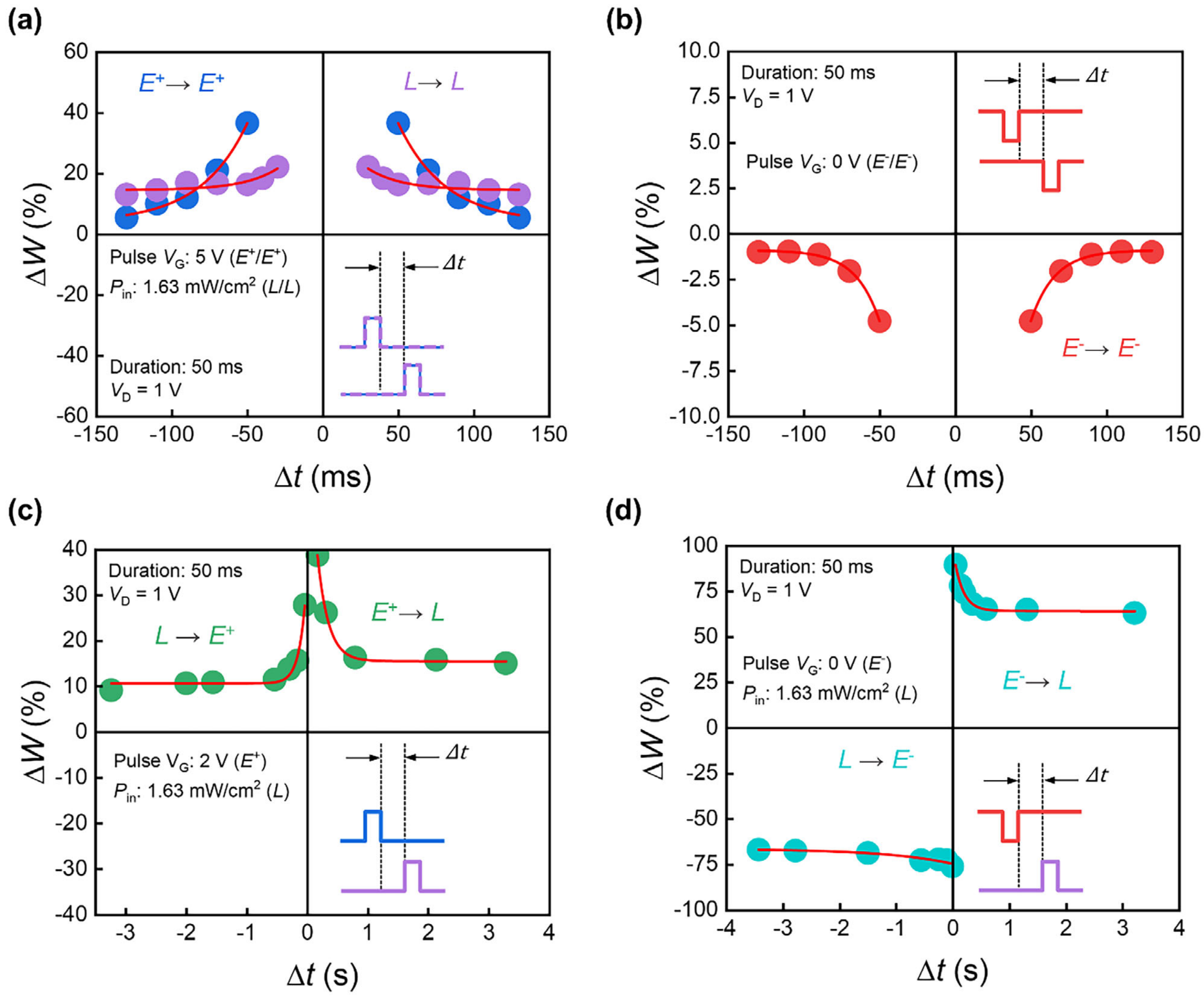

FIGURE 5 | Spike-timing-dependent plasticity (STDP) in the TiO_2-based synaptic phototransistor: dependence of STDP-induced ΔW on interval time between presynaptic and postsynaptic spikes ($\Delta t_{\text{pre-post}}$) in the combinations of (a) L/L and E^+/E^+, (b) E^-/E^-, (c) L/E^+, and (d) E^-/L. The insets show schematic representations of the pre-synaptic and post-synaptic spikes. The P_{in} and pulse V_G conditions used in the acquisition of these measurements are shown in each graph. The pulse duration is 50 ms in all cases.

TABLE 2 | STDP time windows τ (s) of the TiO_2-based synaptic phototransistor.

Pre/Post	L/L	E^+/E^+	E^-/E^-	E^+/L	E^-/L
$\Delta t_{\text{pre-post}} > 0$	22.4 ms	31.0 ms	15.7 ms	180.1 ms	160.2 ms
$\Delta t_{\text{pre-post}} < 0$	22.4 ms	31.0 ms	15.7 ms	115.3 ms	1184.7 ms

match the typical STDP time constants observed in biological synapses, including those in hippocampal and cortical circuits operating on the order of tens of milliseconds [54–56]. This demonstrates that the device is capable of emulating biologically relevant temporal learning windows, under unimodal stimulation conditions. In contrast, the extended τ values observed in the mixed-mode cases (e.g., E^+/L: 180.1 ms, E^-/L: 1184.7 ms) significantly exceed the biological STDP window, suggesting that artificial synapses provide an extended and programmable temporal integration capacity beyond natural constraints. This property could be beneficial for the implementation of long-range temporal correlation learning, delayed associations, or context-dependent modulation in neuromorphic systems.

STDP has been successfully implemented with electrical, optical, and hybrid stimuli, demonstrating the multimodal controllability of synaptic weight changes. The induction of STDP through diverse stimulus combinations enables flexible encoding of temporal correlations, which is very similar to biologically realistic learning rules. This result highlights the potential of the proposed device for unsupervised, time-sensitive learning with local plasticity and offers a promising path toward energy-efficient and autonomous neuromorphic hardware [57].

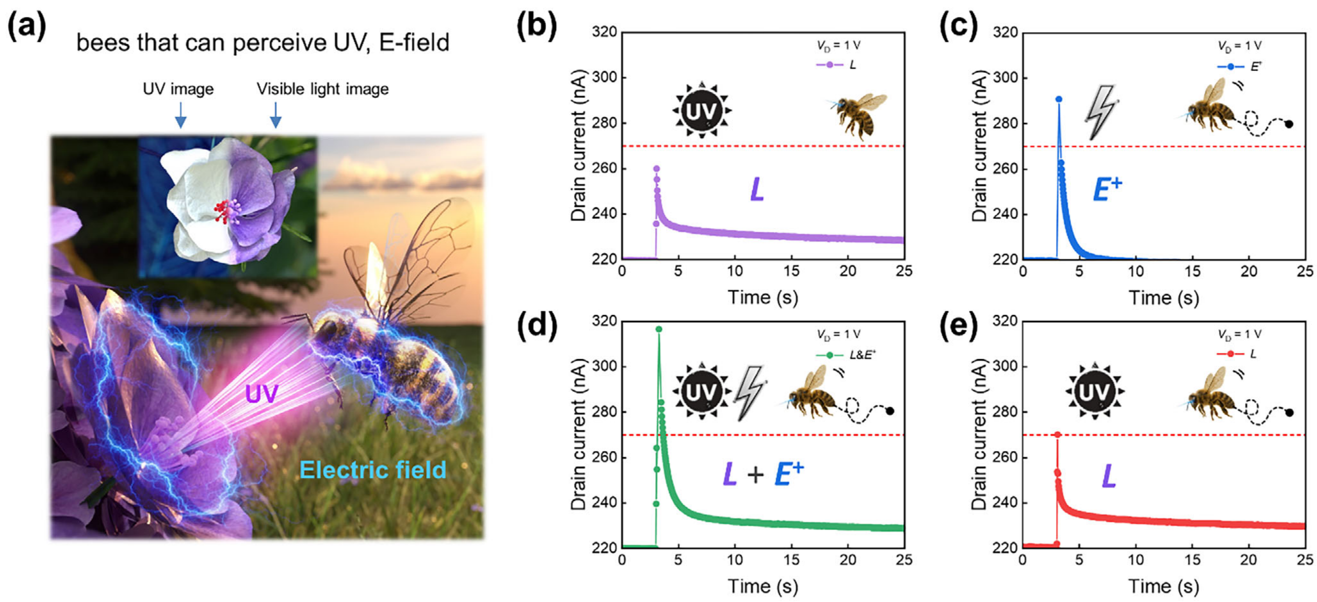

FIGURE 6 | Emulation of associative learning using L and E^+ modes in the TiO_2-based synaptic phototransistor. (a) Schematic illustration of insect-inspired associative conditioning. A bee evaluates the availability of flowers as a reward availability by perceiving UV reflections of the petal and the electric field of the flowers. These biological cues are mapped to the optical (L mode) and electrical (E^+ mode) inputs of the device. (b) Temporal PSC response under stimulation in L mode. The current increases but remains below the predefined threshold (270 nA). (c) PSC response in E^+ mode that exceeds the threshold and triggers a behavioral analog. (d) PSC response with simultaneous L and E^+ stimulation pairing. A strong associative signal is generated that clearly exceeds the threshold. (e) PSC response under stimulation in E^+ mode after the pairing in (d), showing a learned reaction elicited by a single input (after a one-shot associative learning event). The schematic illustration in (a) was originally created for this manuscript as commissioned artwork, and the authors hold the publication rights; no third-party source material or generative AI tools were used.

In future device architectures, delivering optical and electrical stimuli—both positive and negative—through separate terminals (e.g., independent application of light to the gate and voltage to the drain) could enable a broader range of learning patterns and facilitate closer emulation of diverse biological learning behaviors.

The demonstration of associative learning in artificial synapses is an important step toward adaptive neuromorphic systems based on biological principles. In contrast to STP or stimulus-response mapping, it requires the formation and retrieval of causal links between temporally proximal inputs, a process that constitutes a core mechanism of decision making in the animal world. In this paper, such behaviors are modeled using a biologically grounded scenario: how a honeybee identifies nectar-bearing flowers by perceiving UV cues and weak floral electric fields—both well-documented sensory inputs in insect foraging [58, 59].

Figure 6a illustrates this concept schematically. Bees detect UV reflectance patterns of petals and perceive electric fields generated by flowers as cues for nectar availability. In our model, these sensory modalities correspond directly to UV light, with positive gate voltages applied to the synaptic device. In contrast to many previous studies where the applied stimuli bear little resemblance to biological sensory inputs, our approach establishes a direct correspondence in both physical form and biological relevance. Figure 6b–e shows the time-dependent synaptic current responses to different combinations of stimuli, reflecting the progressive stages of associative learning. In Figure 6b, a UV stimulus alone leads to a modest increase in current, but this remains below the predefined trigger threshold (270 nA). This shows the detection of a stimulus without behavioral activation, such as a bee perceiving a floral cue but not initiating an approach. In contrast, Figure 6c shows that a single gate voltage pulse, representing the electric field, induces a current above the threshold, and triggers a response consistent with exploratory behavior. Figure 6d depicts the critical condition, where UV light and gate voltage are applied simultaneously and produce a rapid current rise that clearly exceeds the threshold. The simultaneous occurrence of these two stimuli—each representing a natural sensory signal—facilitates the formation of a stimulus–response association, which is similar to the core principle of classical conditioning. Associative learning is further confirmed in Figure 6e. Following the paired stimulation in Figure 6d, the UV light alone produces a response that exceeds the threshold, even without the input of gate voltage. This indicates that the device has learned to associate the gate stimulus with a reinforced response —a hallmark of successful conditioning.

Such a threshold current in this learning paradigm is comparable to neural responses or behaviors that only occur above a certain activation criterion. Moreover, learning based on two physically distinct but biologically authentic sensory inputs (UV and electric field) distinguishes this result from previous demonstrations of multimodal learning [60, 61]. In particular, replicating not only the functional logic but also the actual sensory pathways used by living organisms increases the biomimetic fidelity of this system. These results emphasize the potential of threshold-driven, multimodal synaptic devices as building blocks for biologically faithful neuromorphic hardware. This approach could be extended to simulate a broader range of sensory inputs beyond light or electrical stimuli, including olfactory or tactile cues.

While demonstrating analog weight modulation at the device level is critical, it is equally important to assess how these characteristics translate into meaningful performance at the system level. The synaptic functionality of the devices was evaluated using practical learning task models. In a convolutional neural network (CNN)-based deep neural network (DNN) architecture (Supporting Information S7), the devices were used to control the weights in a deep layer.

Figure 7b shows two types of multi-level weighting states obtained from over 1,000 pulses, generated either by UV light alone (L) or by simultaneous UV and positive gate voltage (L+E^+) inputs. The dual-stimulus case results in a steeper conductance change, reflecting a stronger potentiation by the combined excitatory effect, whereas the UV-only mode gives a more gradual slope with better linearity. When normalized [39], the linearity index is 0.34 for the UV-only profile, compared to 0.27 for the dual-mode case. This difference has a direct influence on the weighting updates in the network. In early CNN layers, where fast adaptation may be more advantageous than precise control, a steeper but less linear profile could be advantageous. In contract, in deeper or output layers, where fine-grained weight adjustments are critical, a more linear update behavior may provide better performance. The ability to obtain both profiles by simply changing the stimulation conditions allows the device to perform multiple functional roles, favoring dense and energy-efficient neuromorphic systems.

In the CNN architecture trained for digit classification (Supporting Information S7), the three weight update profiles—L, L+E^+—achieved recognition accuracies of 98.37%, 98.39%, respectively. Despite the lower linearity, the L+E^+ mode offers rapid potentiation, while the L-only profile offers consistent performance due to its predictable behavior. To further improve the biological relevance of the system-level evaluation, we additionally performed a flower-related visual recognition simulation under noisy conditions, reflecting the bee-inspired floral-cue scenario introduced in Figure 6. The results further support that TiO_2-based preprocessing enhances noise robustness by preserving salient flower-related features under environmental interference.

Biologically inspired selective attention, which is the ability of organisms to focus on relevant stimuli while filtering out irrelevant background noise has also been studied [62]. For example, honeybees distinguish floral UV patterns and electric fields from environmental distractions such as wind or the surrounding vegetation (Figure 7a) [63]. To emulate this ability, a spiking neural network (SNN) was implemented that includes the temporal integration of the TiO_2 synaptic device as a preprocessing module (Figure 7c). The preprocessing module allows a response to be initiated before the stimulus information is fully transmitted from the sensory cells to the brain cells for processing and decision-making, reducing the time and energy required to respond to stimuli. This is functionally similar to biological attention mechanisms [64]. As shown in Figure 7d, preprocessing consistently improved the SNN accuracy across the tested noise range. The performance gain increased with noise level, reached its maximum at an intermediate noise level (around 0.5), and then gradually diminished as the noise level approached 0.8. These results suggest that our system can emulate the selective attention capabilities of biological organisms by focusing on salient features while suppressing background noise. Figure 7e shows representative images at different noise levels, including the added flower-related visual examples, and illustrates how preprocessing and temporal filtering together enable effective feature extraction under noisy conditions. Considering that TiO_2-based devices can realize both synaptic and neuron (preprocessing) functions, as recently shown by our group [20], this work demonstrates the potential for a fully TiO_2-based hardware system enabled by hardware–software co-design. It demonstrates that diverse synaptic dynamics within a single TiO_2-based platform can be effectively translated from experimentally characterized device behavior to system-level neuromorphic performance. This underscores the importance of jointly optimizing device properties and network architecture for scalable, energy-efficient neuromorphic systems.

3 | Conclusions

In this study, an in situ integrated $TiO_2/SiO_x/Al_2O_3$ synaptic phototransistor possessing multimodal and temporally adaptive neuromorphic functionalities is presented. The device structure was fabricated entirely in-situ using PEALD, ensuring atomic-level uniformity and CMOS-compatible scalability. Optical and electrical synaptic behaviors were successfully emulated by distinct excitation modes—UV-only (L mode), positive gate pulse (E^+ mode), and negative gate pulse (E^- mode)—with reliable excitatory and inhibitory current responses. The proposed device showed important synaptic functions, including EPSC and IPSC behavior, stimulus-dose–dependent synaptic weight modulation, and STDP-like learning. Fine control of the total stimulus dose enabled analog-like weight updates with high resolution. Short- and long-term plasticity were experimentally demonstrated, including PPF and long-term memory transition by repeated stimulation. The time constants extracted from the STDP and PPF measurements were comparable to those observed in biological systems, reinforcing the biorealistic nature of the device. Furthermore, the device enabled associative learning by mimicking the sensory fusion observed in insect behavior, with temporally coordinated UV and electrical stimuli triggering conditioning-like responses. The resulting multimodal weighting functions were validated in a CNN for MNIST digit recognition, achieving up to 98.39% accuracy depending on the weight updating scheme. Furthermore, the experimentally characterized synaptic dynamics were integrated into a SNN, showing improved robustness to noise and selective attention-like functionality at the system level. Taken together, these results establish the TiO_2-based synaptic phototransistor as a compact, reliable, and versatile platform for neuromorphic systems requiring multimodal learning, biologically plausible plasticity, and efficient hardware-software co-optimization.

While the present study demonstrates the essential device- and system-level functionalities, it has thus far been limited to the single-device level, and further investigations are needed to assess large-scale integration and long-term reliability. Moreover, the device was optimized for UV excitation, suggesting that future

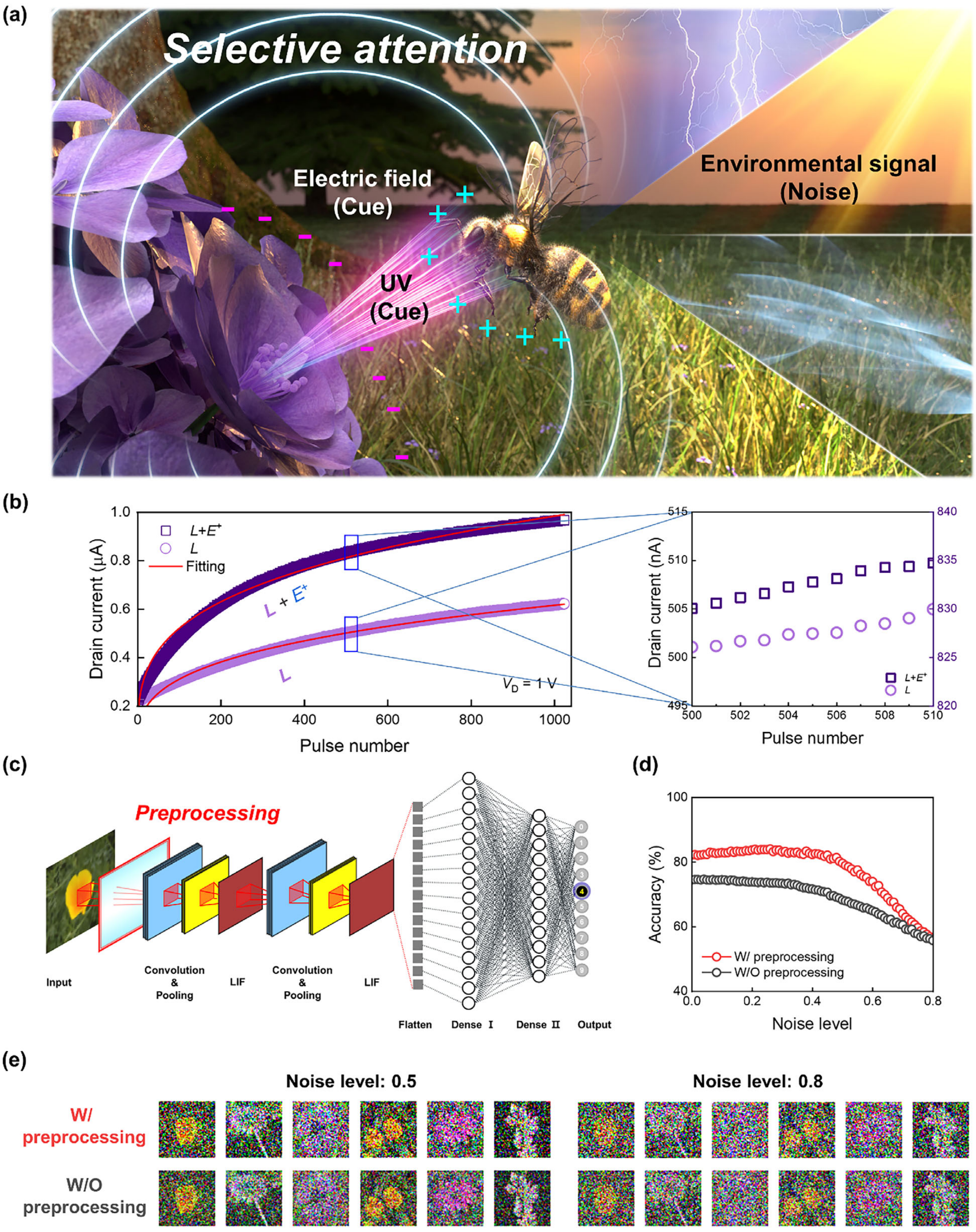

FIGURE 7 | System-level performance evaluation of TiO_2-based synaptic transistors: from analog weight modulation to biologically inspired selective attention and noise-robust classification. (a) Schematic representation of a honeybee showing selective attention during foraging by discriminating salient floral cues (UV pattern and electric field) from environmental noise. (b) Synaptic weight update curves obtained under two stimulation conditions: L and L+E^+ inputs. (c) Architecture of the spiking neural network (SNN) used for noise-robust classification, incorporating TiO_2-based synaptic dynamics. (d) Recognition accuracy as a function of noise level, showing improved robustness at high noise conditions when TiO_2-based synaptic dynamics are used. (e) Examples of input images at different noise levels, showing the effectiveness of preprocessing for selective feature extraction under noisy conditions. The schematic illustration in (a) was originally created for this manuscript as commissioned artwork, and the authors hold the publication rights; no third-party source material or generative AI tools were used.

work should extend the concept to broader spectral ranges and multimodal inputs. Looking ahead, research directions may include the realization of large crossbar arrays, incorporation of diverse sensory modalities, and joint optimization at the device, circuit, and algorithm levels to accelerate the practical deployment of TiO_2-based synaptic phototransistors.

4 | Experimental Section

4.1 | Fabrication Process

The effect of the TiO_2-based synaptic phototransistors on practical learning tasks was evaluated using a convolutional neural network (CNN) training model. A modified National Institute of Standards and Technology (MNIST) handwritten digit dataset was used, consisting of 48 000 images for training, 12 000 for validation, and 10 000 for testing.

On highly doped n^{++}-Si substrates, which were also used as the bottom gate electrodes. First, the dual gate dielectric and channel layers were deposited in situ using a PEALD process at 300°C. High-purity Ar was used as both carrier and purge gas. The dual gate dielectric consisted of a 5 nm thick Al_2O_3 layer and a 25 nm thick charge-inducing dielectric, whereas a 28 nm thick TiO_2 layer was deposited as the channel. Subsequently, to pattern the channel layer, AZ5214 photoresist was spin-coated using a spin coater, followed by photolithography with a contact aligner. Reactive-ion etching (RIE) was then performed, and residual photoresist was removed by acetone sonication for 10 min. The width/length of the channel was 40/15 µm. Following a process analogous to the channel patterning, photoresist coating and photolithography were performed to define the source and drain patterns. Then, source and drain electrodes made of aluminum with a thickness of approximately 230 nm were deposited using E-beam evaporation with a deposition rate of 3–4 Å/s. Finally, a lift-off process using acetone was performed to remove the residual Al.

4.2 | Characterization of the Devices

The thickness and crystal structure of the TiO_2-based synaptic phototransistors were investigated using TEM (Tecnai G2 F30 Super-Twin, FEI, United States) at 300 keV. Sampling to acquire cross-sectional information was performed using a focused ion beam milling system (Helios NanoLab, Thermo Fisher, United States). FFT patterns were generated using a Gatan DigitalMicrograph (AMETEK, Inc., United States) to analyze the crystal structure. The transmittance of the TiO_2 layer was determined using a spectrophotometer for ultraviolet, visible, and near infrared light (Lambda 1050, Perkin Elmer, United States). Electrical characterization, including both fundamental and synaptic properties, was performed using a semiconductor parameter analyzer (Keithley 4200-SCS, Tektronix, United States). Optical stimulation input was provided by a light-emitting device (LED) light source (WLS-22-A, Mightex, Canada). The LED optical pulses were controlled with a light source control module (BLS-PL04-US, Mightex, Canada). Measurements were performed at room temperature within a light-shielded control box to eliminate the effects of ambient light. For long-term storage stability evaluation, the devices were stored under ambient laboratory conditions at room temperature without encapsulation or special light-shielded storage.

4.3 | Evaluation Using Learning Models

The effect of TiO_2-based synaptic phototransistors on practical learning tasks was evaluated using neural network training and inference models. A convolutional neural network (CNN)-based spiking neural network (SNN) model was used in this study with a modified National Institute of Standards and Technology (MNIST) handwritten digit dataset consisting of 48 000 images for training, 12 000 for validation, and 10 000 for testing. The simulations were implemented in a Google Colab environment using Python with PyTorch and snnTorch, while NumPy and Matplotlib were used for data processing and visualization. For the SNN input, rate coding proportional to the probability distribution of the image data of the handwritten digits—quantized in 256 levels between 0 and 1—was applied, and artificial leaky integrate-and-fire (LIF) neurons were used. For the deep neural network, inference accuracy was evaluated under the assumption that the TiO_2-based synaptic phototransistors operated by programming the weights of the deep layer, taking into account the linearity index of each L or E^+/E^- stimuli (Supporting Information S7).

In addition, a CNN-based SNN was implemented for binary flower/non-flower image classification. Flower images were collected from the Oxford 102 Flowers dataset, whereas non-flower images were selected from several object categories in the CIFAR-10 dataset. All RGB images were resized to 64 × 64 pixels and normalized to the range of 0–1 before training and testing. For SNN processing, rate coding based on the normalized pixel-intensity distribution of the RGB images was employed together with artificial LIF neurons.

To use the TiO_2-based synaptic phototransistors in the SNN, a preprocessing stage consisting of TiO_2-based synaptic phototransistors and LIF neurons was placed in the input layer. In the simulations, the response of the TiO_2 devices was modeled with a function similar to the experimentally measured PPF characteristics. Gaussian noise was randomly added to the input from each pixel of a handwritten digit image (with the noise level defined as the standard deviation of the Gaussian noise), and the accuracy of the inference was assessed by varying the LIF threshold of the preprocessing stage.

For the flower/non-flower classification task, noisy RGB input images were first transformed into spike maps using the TiO_2-based LIF preprocessing module before being applied to the SNN.

Acknowledgements

This work was supported by the Technology Innovation Program (00405151) funded by the Ministry of Trade, Industry & Energy (MOTIE, Korea), by the Electronics and Telecommunications Research Institute (ETRI) grant funded by the Korean government [26ZB1330], and by the National Research Foundation of Korea (NRF) grant funded by the Korean government (MSIT) (No. RS-2024-00352660).

Conflicts of Interest

The authors declare no conflicts of interest.

Data Availability Statement

The data that support the findings of this study are available from the corresponding author upon reasonable request.

References

1. D. R. Muir and S. Sheik, "The Road to Commercial Success for Neuromorphic Technologies," *Nature Communications* 16 (2025): 3586, https://doi.org/10.1038/s41467-025-57352-1.

2. S. S. Chowdhury, D. Sharma, A. Kosta, and K. Roy, "Neuromorphic Computing for Robotic Vision: Algorithms to Hardware Advances," *Communications Engineering* 4 (2025): 152, https://doi.org/10.1038/s44172-025-00492-5.

3. J. Tang, F. Yuan, X. Shen, et al., "Bridging Biological and Artificial Neural Networks With Emerging Neuromorphic Devices: Fundamentals, Progress, and Challenges," *Advanced Materials* 31 (2019): 1902761, https://doi.org/10.1002/adma.201902761.

4. B. He, B. Bao, R. Martins, S. Wang, and G. He, "Frame-Channel Engineered Multimodal Transistor Integrating Neuromorphic Computing With Cross-Modal Edge Intelligence," *Advanced Functional Materials* 35 (2025): 2506332, https://doi.org/10.1002/adfm.202506332.

5. X. Zhang, J. Zhou, Y. Zhang, et al., "Implementing Multimodal Hardware Security With 2D α-In_2Se_3 Ferroelectric Transistor," *Advanced Science* 12 (2025): 2502286, https://doi.org/10.1002/advs.202502286.

6. J. Liu, M. Zhang, W. Han, F. Du, L. Wu, and X. Fang, "Ferroelectric-Gated Hybrid-Layered Organic Field-Effect Transistors for Multimode Signal Processing," *Advanced Functional Materials* 36 (2025): 08765, https://doi.org/10.1002/adfm.202508765.

7. Y. Yoon, Y. Kim, S. Choi, J. Kwon, and M. Shin, "Synaptic a-Si:H/a-Ga2O3 Phototransistor Inspired by the Phototaxis Behavior of Organisms With All-Optical and All-Electrical Stimulation Modes," *Nano Research* 17 (2024): 7631–7642, https://doi.org/10.1007/s12274-024-6754-7.

8. Y. Yoon, Y. Kim, W. S. Hwang, and M. Shin, "Biological UV Photoreceptors-Inspired Sn-Doped Polycrystalline β-Ga*2O3* Optoelectronic Synaptic Phototransistor for Neuromorphic Computing," *Advanced Electronic Materials* 9 (2023): 2300098, https://doi.org/10.1002/aelm.202300098.

9. J. Yao, Y. Teng, Q. Wang, et al., "Advancing Intelligent Neuromorphic Computing: Recent Progress in All-Optical-Controlled Artificial Synaptic Devices," *ACS Nano* 19 (2025): 26320–26346, https://doi.org/10.1021/acsnano.5c05240.

10. F. Su, Z. Wang, J. Wan, and D. Wang, "Recent Advances in Optoelectronic Synapses: From Advanced Materials to Neuromorphic Applications," *Rare Metals* 32 (2025): 6807–6838, https://doi.org/10.1007/s12598-025-03433-5.

11. Z. Yang, Z. Zhang, S. Huo, et al., "Emerging 2D Material-Based Synaptic Devices: Principles, Mechanisms, Improvements, and Applications," *Smart Mat* 2 (2025): 70005, https://doi.org/10.1002/smm2.70005.

12. Y. J. Du, J. Yang, Z. Lv, et al., "Integration of Perovskite/Low-Dimensional Material Heterostructures for Optoelectronics and Artificial Visual Systems," *Advanced Functional Materials* 35 (2025): 2500953, https://doi.org/10.1002/adfm.202500953.

13. W. Zhang, S. li, C. Zhang, J. Shang, M. Ma, and D. Ma, "Recent Advances in Heterostructure-Based Organic Field-Effect Transistor Memory," *Nanoscale* 17 (2025): 20643–20669, https://doi.org/10.1039/D5NR01954K.

14. Q. Fan, J. Shang, X. Yuan, Z. Zhang, and J. Sha, "Emerging Liquid-Based Memristive Devices for Neuromorphic Computation," *Small Methods* 9 (2025): 2402218, https://doi.org/10.1002/smtd.202402218.

15. R. Zhao, S. J. Kim, Y. Xu, et al., "Memristive Ion Dynamics to Enable Biorealistic Computing," *Chemical Reviews* 125 (2025): 745, https://doi.org/10.1021/acs.chemrev.4c00587.

16. G. Kumar, A. Paul, A. Das, G. Larrieu, and S. De, "Insights Into Oxygen Vacancy Effects on Ferroelectric Behavior of Hafnium Oxide: A Review," *Physica Status Solidi (a)* 222 (2025): 2500376, https://doi.org/10.1002/pssa.202500376.

17. J. Y. Mao, S. Wu, G. Ding, et al., "A van der Waals Integrated Damage-Free Memristor Based on Layered 2D Hexagonal Boron Nitride," *Small* 18 (2022): 2106253, https://doi.org/10.1002/smll.202106253.

18. S. Kumar, Z. Wang, X. Huang, et al., "Oxygen Migration During Resistance Switching and Failure of Hafnium Oxide Memristors," *Applied Physics Letters* 110 (2017): 103503, https://doi.org/10.1063/1.4974535.

19. M. K. Afshar and E. Nadimi, "Defect-Mediated Resistive Switching in Thin Multilayer Hexagonal Boron Nitride: A First Principles Study of Charge State Modulation," *Materials Today Physics* 52 (2025): 101673, https://doi.org/10.1016/j.mtphys.2025.101673.

20. J. Lee, J. W. Lim, and C. Park, "Solely Light-Induced Integrate-and-Fire 1T-Neuron Operation and Implementation of the McGurk Effect," *Small Structures* 6 (2025): 2400522, https://doi.org/10.1002/sstr.202400522.

21. C. Park and J. W. Lim, "Light-Induced Radix Modulation and Optoelectronic Synaptic Properties in Ternary-Logic Devices," *Small Structures* 6 (2025): 2400530, https://doi.org/10.1002/sstr.202400530.

22. J. Kim, J. W. Lim, and H. S. Kim, "Synaptic Devices for Simulating Brain Processes in Visual-Information Perception to Persisting Memory Through Attention Mechanisms," *Materials Today Advances* 20 (2023): 100421, https://doi.org/10.1016/j.mtadv.2023.100421.

23. J. W. Lim, S. J. Heo, M. A. Park, and J. Kim, "Synaptic Transistors Exhibiting Gate-Pulse-Driven, Metal-Semiconductor Transition of Conduction," *Materials (Basel)* 14 (2021): 7508, https://doi.org/10.3390/ma14247508.

24. M. Zahid, M. I. Sadiq, C. Jin, et al., "Nitrogen-Doped Carbon Quantum Dot-Decorated In_2O_3 Synaptic Transistors for Neuromorphic Computing," *Applied Physics Letters* 125, no. 19 (2024): 193503, https://doi.org/10.1063/5.0231655.

25. C. Jin, W. Liu, Y. Huang, et al., "Printable Ion-Gel-Gated In_2O_3 Synaptic Transistor Array for Neuro-Inspired Memory," *Applied Physics Letters* 120, no. 23 (2022): 233701, https://doi.org/10.1063/5.0092968.

26. L. Zhu, J. Ding, F. Zhang, et al., "Low-Temperature Solution-Processed In_2O_3 Synaptic Transistors for Dual-Light Visual Perception and Neuromorphic Computing," *IEEE Transactions on Electron Devices* 73 (2025): 382–387, https://doi.org/10.1109/TED.2025.3638295.

27. X. Li, L. Yi, X. Yin, J. Cheng, Q. Xin, and A. Song, "Fully Screen-Printed Paper-Based ZnO Synaptic Transistor Arrays for Visual Perception and Neuromorphic Computing," *NPJ Flexible Electronics* 9, no. 1 (2025): 57, https://doi.org/10.1038/s41528-025-00425-4.

28. R. Oommen, D. S. Ganapathi Mavuri, K. Jose, and A. R. Nair, "Tunable Memory Behavior in Light Stimulated Artificial Synapse Based on ZnO Thin Film Transistors," *Journal of Physics D: Applied Physics* 57, no. 46 (2024): 465102, https://doi.org/10.1088/1361-6463/ad6dff.

29. J. Lin, S. Lan, L. Yang, Q. Lin, Y. Chen, and W. Xu, "Na-Doped Ga_2O_3 Electrolyte-Gated Synaptic Transistors for Neuromorphic Computing," *Journal of Materials Chemistry C* 13 (2025): 13246–13254, https://doi.org/10.1039/D5TC01248A.

30. J. Kim, A. Kumar, J. Kim, et al., "High Power Operating Neuromorphic Transistor Based on F-Doped β-Ga_2O_3 Channel on Si Wafers," *Journal of Alloys and Compounds* 1039 (2025): 183267, https://doi.org/10.1016/j.jallcom.2025.183267.

31. P. Li, J. Shi, Z. Li, et al., "Boosting Performance of Ga_2O_3 Thin-Film Transistors via Defect Passivation Toward Solar-Blind Ultraviolet In-Sensor Reservoir Computing," *ACS Nano* 20 (2025): 1420–1430, https://doi.org/10.1021/acsnano.5c18136.

32. H. Qu, H. Du, Y. Zhu, et al., "Voltage-Controlled Reconfigurable Boolean Logic Enabled by a β-Ga_2O_3 Artificial Optoelectronic Synapse," *ACS Applied Electronic Materials* 7 (2025): 9792–9800, https://doi.org/10.1021/acsaelm.5c01613.

33. G. Ma, R. Yan, and H. Tang, "Exploiting Noise as a Resource for Computation and Learning in Spiking Neural Networks," *Patterns* 4 (2023): 100831, https://doi.org/10.1016/j.patter.2023.100831.

34. Z. Wang, S. Li, and G. Shen, "Advanced Sensory Hardware for Intelligent Eye-Machine Interfacing: From Wearables to Bionics," *Advanced Functional Materials* 35 (2025): 2503519, https://doi.org/10.1002/adfm.202503519.

35. R. Midya, A. S. Pawar, D. P. Pattnaik, et al., "Artificial Transneurons Emulate Neuronal Activity in Different Areas of Brain Cortex," *Nature Communications* 16 (2025): 7289, https://doi.org/10.1038/s41467-025-62151-9.

36. M. Evanusa and Y. Sandamirskaya, "Event-Based Attention and Tracking on Neuromorphic Hardware," in *Proceedings of the IEEE/CVF Conference on Computer Vision and Pattern Recognition Workshops* (2019), 0.

37. G. Brauwers and F. Frasincar, "A General Survey on Attention Mechanisms in Deep Learning," *IEEE Transactions on Knowledge and Data Engineering* 35 (2023): 3279–3298, https://doi.org/10.1109/TKDE.2021.3126456.

38. M. Yao, G. Zhao, H. Zhang, et al., "Attention Spiking Neural Networks," *IEEE Transactions on Pattern Analysis and Machine Intelligence* 45 (2023): 9393–9410, https://doi.org/10.1109/TPAMI.2023.3241201.

39. J. W. Lim, M. A. Park, and J. Kim, "Photo-Synaptic Oxide Transistors With Al_2O_3/SiO_x Stacked Gate Dielectric Exhibiting 1024 Conduction States With Good Linearity," *Advanced Electronic Materials* 8 (2022): 2200494, https://doi.org/10.1002/aelm.202200494.

40. H. Tang, K. Prasad, R. Sanjinès, P. E. Schmid, and F. Lévy, "Electrical and Optical Properties of TiO_2 Anatase Thin Films," *Journal of Applied Physics* 75 (1994): 2042–2047, https://doi.org/10.1063/1.356306.

41. Y. S. Kim, H. J. Jin, H. R. Jung, et al., "Reduced Extrinsic Recombination Process in Anatase and Rutile TiO_2 Epitaxial Thin Films for Efficient Electron Transport Layers," *Scientific Reports* 11 (2021): 6810, https://doi.org/10.1038/s41598-021-86422-9.

42. Y. Leprince-Wang and K. Yu-Zhang, "Study of the Growth Morphology of TiO_2 Thin Films by AFM and TEM," *Surface and Coatings Technology* 140 (2001): 155–160, https://doi.org/10.1016/S0257-8972(01)01029-5.

43. D. Mardare, M. Tasca, M. Delibas, and G. I. Rusu, "On the Structural Properties and Optical Transmittance of TiO_2 r.f. Sputtered Thin Films," *Applied Surface Science* 156 (2000): 200, https://doi.org/10.1016/S0169-4332(99)00508-5.

44. J. Kim, J. W. Lim, and J. Lee, "Characteristics of PEALD–Hafnium Dioxide Films and their Application to Gate Insulator Stacks of Photosynaptic Transistors," *Advanced Electronic Materials* 8 (2022): 2101061, https://doi.org/10.1002/aelm.202101061.

45. D. M. Fleetwood, "1/f Noise and Defects in Microelectronic Materials and Devices," *IEEE Transactions on Nuclear Science* 62 (2015): 1462–1486, https://doi.org/10.1109/TNS.2015.2405852.

46. S. K. Tewksbury, "Relaxation Effects in MOS Devices Due to Tunnel Exchange With Near-Interface Oxide Traps," (PhD diss., MIT, 1992).

47. P. Dutta and P. M. Horn, "Low-Frequency Fluctuations in Solids: 1/f noise," *Reviews of Modern Physics* 53 (1981): 497–516, https://doi.org/10.1103/RevModPhys.53.497.

48. W. T. Xu, S. Y. Min, H. Hwang, and T. W. Lee, "Organic Core-Sheath Nanowire Artificial Synapses With Femtojoule Energy Consumption," *Science Advances* 2 (2016): 1501326, https://doi.org/10.1126/sciadv.1501326.

49. S. B. Laughlin and T. J. Sejnowski, "Communication in Neuronal Networks," *Science* 301 (2003): 1870–1874, https://doi.org/10.1126/science.1089662.

50. R. S. Zucker and W. G. Regehr, "Short-Term Synaptic Plasticity," *Annual Review of Physiology* 64 (2002): 355–405, https://doi.org/10.1146/annurev.physiol.64.092501.114547.

51. R. Yang, H. M. Huang, Q. H. Hong, et al., "Synaptic Suppression Triplet-STDP Learning Rule Realized in Second-Order Memristors," *Advanced Functional Materials* 28 (2018): 1704455, https://doi.org/10.1002/adfm.201704455.

52. N. Caporale and Y. Dan, "Spike Timing–Dependent Plasticity: A Hebbian Learning Rule," *Annual Review of Neuroscience* 31 (2008): 25–46, https://doi.org/10.1146/annurev.neuro.31.060407.125639.

53. R. C. Froemke and Y. Dan, "Spike-Timing-Dependent Synaptic Modification Induced by Natural Spike Trains," *Nature* 416 (2002): 433–438, https://doi.org/10.1038/416433a.

54. G. Q. Bi and M. M. Poo, "Synaptic Modifications in Cultured Hippocampal Neurons: Dependence on Spike Timing, Synaptic Strength, and Postsynaptic Cell Type," *The Journal of Neuroscience* 18 (1998): 10464–10472, https://doi.org/10.1523/JNEUROSCI.18-24-10464.1998.

55. P. J. Sjöström and S. B. Nelson, "Spike Timing, Calcium Signals and Synaptic Plasticity," *Current Opinion in Neurobiology* 12 (2002): 305, https://doi.org/10.1016/S0959-4388(02)00325-2.

56. J. C. Zhang, P. M. Lau, and G. Q. Bi, "Gain in Sensitivity and Loss in Temporal Contrast of STDP by Dopaminergic Modulation at Hippocampal Synapses," *Proceedings of the National Academy of Sciences* 106 (2009): 13028–13033, https://doi.org/10.1073/pnas.0900546106.

57. G. Srinivasan, P. Panda, and K. Roy, "STDP-Based Unsupervised Feature Learning Using Convolution-Over-Time in Spiking Neural Networks for Energy-Efficient Neuromorphic Computing," *ACM Journal on Emerging Technologies in Computing Systems* 14 (2018): 1–12, https://doi.org/10.1145/3266229.

58. M. Giurfa, J. Nunez, L. Chittka, and R. Menzel, "Colour Preferences of Flower-Naive Honeybees," *Journal of Comparative Physiology A* 177 (1995): 247, https://doi.org/10.1007/BF00192415.

59. D. Clarke, H. Whitney, G. Sutton, and D. Robert, "Detection and Learning of Floral Electric Fields by Bumblebees," *Science* 340 (2013): 66–69, https://doi.org/10.1126/science.1230883.

60. R. Li, Z. Yue, H. Luan, Y. Dong, X. Chen, and M. Gu, "Multimodal Artificial Synapses for Neuromorphic Application," *Research* 7 (2024): 0427, https://doi.org/10.34133/research.0427.

61. L. Fang, C. Mao, H. Wang, et al., "Recent Progress of Organic Artificial Synapses in Biomimetic Sensory Neural Systems," *Journal of Materials Chemistry C* 12 (2024): 8586–8610, https://doi.org/10.1039/D4TC00704B.

62. V. Nityananda, "Attention-Like Processes in Insects," *Proceedings of the Royal Society* 283 (2016): 20161986, https://doi.org/10.1098/rspb.2016.1986.

63. S. Ravi, J. E. Garcia, C. Wang, and A. G. Dyer, "The Answer Is Blowing in the Wind: Free-Flying Honeybees Can Integrate Visual and Mechano-Sensory Inputs for Making Complex Foraging Decisions," *Journal of Experimental Biology* 219 (2016): 3465, https://doi.org/10.1242/jeb.142679.

64. X. Qiu, R. J. Zhu, Y. Chou, Z. Wang, L. J. Deng, and G. Li, "Gated Attention Coding for Training High-Performance and Efficient Spiking Neural Networks," *Association for Advancement of Artificial Intelligence* 38, no. 1 (2024): 601–610, https://doi.org/10.1609/aaai.v38i1.27816.

Supporting Information

Additional supporting information can be found online in the Supporting Information section.

Supporting File: admt71152-sup-0001-SuppMat.docx.